NeuroCSF: an fMRI method to measure contrast sensitivity function in human visual cortex

Laurie Goulet, and Reza Farivar

Department of Ophthalmology & Visual Sciences, McGill University, Montreal, Canada

Address correspondence to Reza Farivar. Email: reza.farivar@mcgill.ca

Acknowledgements: This research was partly supported by CIHR under Grant Number 899956. The authors declare no competing interests.

Abstract

The contrast sensitivity function (CSF) describes a range of spatial frequencies (SF) that are detectable at a given level of contrast and is a very valuable tool both in clinical and fundamental research. However, despite its immense value, the full potential of the CSF has not been utilized in every aspect of clinical research due to time limits and patient factors. We propose neuroCSF as a new method for measuring the CSF across the visual field directly from brain activity, and with minimal demand from participants. NeuroCSF is a computational model that estimates voxel-wise CSF parameters (i.e., peak contrast sensitivity, peak spatial frequency, and spatial frequency bandwidth) from functional magnetic resonance imaging (fMRI) signals, under controlled visual stimulation conditions. The approach extends the population spatial frequency tuning (Aghajari, Vinke, & Ling, 2020) and population receptive field (Dumoulin & Wandell, 2008) methods to provide the first characterization of a full CSF using neuroimaging. We observe that across early visual areas (V1, V2 and V3), the CSF peak spatial frequency and spatial frequency cutoff are significantly higher for foveal eccentricity and decrease at parafoveal eccentricities. Conversely, SF bandwidth slowly increases with eccentricity, while peak contrast sensitivity remains constant with eccentricity for all early visual areas. Thus, cortical CSF estimates vary systematically with eccentricity. The neuroCSF approach opens new perspectives for the study of cortical visual functions in various disorders where the CSF is impacted, such as amblyopia, traumatic brain injury, and multiple sclerosis.

Introduction

The Contrast Sensitivity Function (CSF), originally developed by Campbell and Robson [1] describes the range of spatial frequencies detectable at varying levels of contrast. It is widely

acknowledged as the gold standard for evaluating visual performance. The CSF not only serves to delineate the boundary between perceptually visible and invisible stimuli but also sheds light on the limiting factors affecting everyday functional vision [2, 3].

The CSF predicts visual target recognition in everyday life, encompassing tasks such as recognizing faces [4-6], interpreting road signs [4], deciphering letters, and performing real-world visual tasks like reading, driving, and mobility [7-10]. Its ability to assess the visual system's sensitivity to different levels of contrast provides crucial information about the overall health and functioning of the system. In clinical visual sciences [11], the CSF holds a vital place, serving as a non-invasive assessment tool for the detection and tracking of visual impairments originating from ocular diseases or neurological deficits. Below, we briefly discuss the clinical concerns for which CSF can be valuable (amblyopia, age-related macular degeneration, and multiple sclerosis) and speculate on a fourth—post-concussive visual blur.

Amblyopia, commonly known as "lazy eye", is characterized by reduced visual acuity in an otherwise healthy eye and is often resulting from abnormal visual experience in early childhood. It is traditionally diagnosed with visual acuity tests, but losses in contrast sensitivity have been detected in amblyopes with reported normal visual acuity [12]. Studies report significant contrast sensitivity reductions in both the treated amblyopic eye (AE) and fellow-fixing eye (FE) of "cured" amblyopic subjects when compared to control subjects [13, 14]. Analyzing the CSF could thus aid in the detection and monitoring of amblyopia, providing insights into visual symptoms that go beyond acuity measurements.

Age-related macular degeneration (AMD) is a progressive retinal disease that primarily affects the central portion of the retina that is responsible for detailed vision. It is one of the leading causes of vision impairments in the elderly [15]. Early changes of AMD are predominantly

morphological and often occur without noticeable or measurable vision loss symptoms. Conventional clinical tests, such as visual acuity, often miss these early subtle changes, limiting their clinical utility in early and intermediate stages of AMD [16-18]. Measuring early functional changes in AMD poses significant challenges and the CSF could be instrumental in tracking functional vision loss associated with AMD [19]. In its early stage, AMD results in a CSF that is similar in shape to the normal population, but that is shifted along both axes [20, 21]. As the disease progresses, the CSF can reveal specific patterns of deficits within the visual field, allowing clinicians to tailor interventions and monitor their effectiveness.

Multiple sclerosis (MS), a disorder involving demyelination of the central nervous system, is commonly manifested early on by ocular symptoms. Findings suggest that MS involves contrast sensitivity deficits that precede changes in visual acuity [22-24]. A recent study by Nunes, Monteiro and Vaz Pato [25] revealed that in its early stages, MS can produce highly selective contrast sensitivity loss for high spatial frequencies. As the disease progresses, greater losses are seen in the low-frequencies band. By assessing the contrast sensitivity function, clinicians can identify early signs of MS in patients and track the progression of the disease.

While CSF degradation has been often considered in light of optical or ocular losses, in at least one case—post-traumatic visual blur—the eyes and the optics appear normal but patients report persistent “blur” [26, 27]. Because this type of blur cannot be readily explained by ocular or optical factors, it necessitates neurological measures of the CSF, which currently do not exist.

The major problem faced is that despite its immense value, the full potential of the CSF has not been utilized in every aspect of clinical research, due to several challenges associated with standard psychophysical CSF techniques, including time constraints, patient-related issues, and technique limitations.

One of the primary challenges comes from the substantial time required to perform a full CSF assessment at one retinal location (typically foveal), ranging from 15 to 30 minutes per eye. This duration that already poses as a challenge for healthy participants can become almost impossible to perform for a patient that also suffers from attention and/or fixation problems, visual discomfort, or mobility issues [28, 29]. Behavioral CSF measures are also affected by extraneous factors such as fatigue, compliance, attention [30, 31], emotional arousal [32] and feedback adaptation[33].

Crucially, CSF measures are typically done at one retinal location—foveally. In certain visual deficits like amblyopia or age-related macular degeneration, visual impairments vary *across* the visual field [34-36]. Currently to obtain information about such visual field distinctions, the CSF must be behaviorally tested at multiple positions, which poses challenges for both healthy and clinical participants. This is why the standard laboratory methods for measuring the CSF have not been used to their full potential in clinical research.

In recent years, various alternative approaches to psychophysical CSF measurement have been proposed, but often at the cost of efficiency or validity. For instance, Visual Evoked Potentials (VEPs) offer objectivity but vary in sensitivity [37-39]. Similarly, methods relying on eye movements, such as Gradiate [40] or optokinetic nystagmus (OKN) [41, 42], are reliable approaches that can be used with children or individuals with cognitive deficits, but vary in complexity and efficacy, and fail to account for retinal location differences.

The CSF is a promising tool that can quantify subtle patterns of visual deficits that may otherwise go unrecognized by current testing methods and provides information relevant for disease progression and monitoring of treatment efficacy. Existing tools have a number of constraints, mainly demanding extensive behavioural compliance and limited assessment at

multiple retinal locations. We sought to overcome these challenges to develop an objective measure of the CSF across the visual field with minimal behavioural demands on the patient.

We have developed the neuroCSF, a method for directly estimating the CSF across the visual field from functional Magnetic Resonance Imaging (fMRI) signals. The neuroCSF objectively estimates voxel-wise CSF parameters, including peak contrast sensitivity, peak spatial frequency, and spatial frequency bandwidth. This estimation process relies on a modeling approach that translates the behavioral CSF model into a neural one.

The neuroCSF offers a substantial advantage over traditional approaches by simultaneously measuring all visual field locations within an eccentricity limit in under 35 minutes of scan time (and potentially much shorter, with further optimizations). It provides unbiased measures of the CSF for each voxel across the visual brain without requiring input from participants. This transformative method represents a significant advancement in CSF measurement, offering an objective, fixation-independent, and non-invasive method to simultaneously assess the entire visual field.

Materials and Methods

Subjects

Eight subjects with normal or corrected-to-normal vision (3 males; mean age, 27; range, 22-32 years) were recruited for this experiment. The participants had no prior history of binocular dysfunction. Informed consent was obtained from each subject in accordance with the Code of Ethics of the World Medical Association (Declaration of Helsinki) and was approved by the Research Ethics Board of the McGill University Health Center.

Imaging

Display

Stimuli were generated using Psychtoolbox [43] through MATLAB (2019a, The Math Works Inc., Natick, Massachusetts) and displayed on a gamma-corrected 32" LCD BOLDScreen (Cambridge Research Systems) at 120Hz with a mean luminance of 120 cd/m^2 reflected by a mirror above the participant's head. Participants were placed at a viewing distance of 152 cm from the monitor spanning 25.8 by 14.7 degrees of visual angle at a pixel resolution of 1920 by 1080. All stimuli were viewed binocularly.

Equipment/setup

Acquisition was performed on a Siemens Prisma 3T MRI Scanner at the Montreal General Hospital (McGill University Health Center). Functional images were acquired using a 32-channel vision coil [44] in a transverse plane perpendicular to the calcarine sulcus with a standard simultaneous multislice (SMS) echo-planar imaging (EPI) sequence (Resolution = 2 x 2 x 2 mm, TR= 1000ms, TE: 33ms, FA= 33°, fat saturation, FOV = 128 x 128 mm, number of slices= 16, R=2, BW = 1698 Hz/pixel). Anatomical images were obtained with a 64-channel head coil using a T1-weighted magnetization prepared-rapid gradient echo (MPRAGE) sequence (Resolution = 0.8mm3, TR= 1780ms, TE=2.64ms, FA = 9o, FOV = 216 x 216 mm, number of slices= 208).

Preprocessing of Functional Images

Preprocessing of fMRI data was performed using Analysis of Functional NeuroImages (AFNI) [45]. To minimize spatial blurring, all spatial transformations following slice-time correction (i.e., motion correction, distortion correction, registration to anatomical image) were applied in a single step. Preprocessing of the T1-weighted anatomical images for alignment with the functional images was performed using Freesurfer (http://surfer.nmr.mgh.harvard.edu/).

NeuroCSF Stimuli & Experimental Procedure

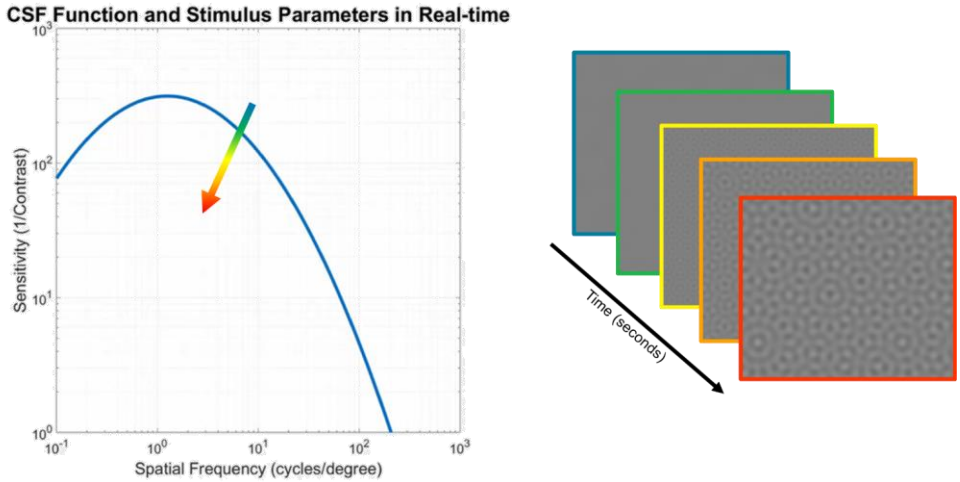

Figure 1. Stimulus presentation sequence for the CSF modeling. *Depiction of one transition of the full field dynamic stimuli that varies over time in spatial frequency and contrast (right). The five frames depicted are only a subset of the 300 frames that would be presented within one of the 20 stimulus transitions. The stimulus consists of a contrast and spatial frequency vector (left) and any of its time points represent a shift in this two-dimensional space of contrast and spatial frequency.*

During the functional runs, we binocularly presented full-field stimuli that varied systematically in contrast (min=10 % max=60%) and spatial frequency (min=0.033 cycles/degree [cpd], max=26cpd). Stimuli were generated by overlapping eight sinusoidal gratings with evenly spaced rotations over 180°, making the stimuli not selective for any orientation.

Each run included 20 ten-second periods of smoothly transitioning contrast-spatial frequency vectors—crossing from the subthreshold to suprathreshold regimes of the CSF (Fig. 1)—presented in a random sequence. The crossing points were evenly spaced (logarithmically) across the expected range in the contrast-spatial frequency space. This smoothly dynamic stimuli strategy ensured that we would capture activity, as measured through the blood oxygen level-dependent (BOLD) response via fMRI, as it transitioned from zero response—when the stimulus was subthreshold—to complete activation—when the stimulus was suprathreshold. We thus captured the experience of an entire transition from subthreshold to suprathreshold and observed the changes in neural activity as the brain began to detect the stimuli

Each stimulus presentation was followed by a blank interstimulus interval defined by a Gaussian distribution with a mean of 5s. To help with attention, participants were instructed to report whenever they perceived the stimuli by pressing a key. Each session comprised of three unique runs, with the same trajectories but shown in different orders, repeated twice, totaling approximately 30 minutes.

NeuroCSF Data Analysis

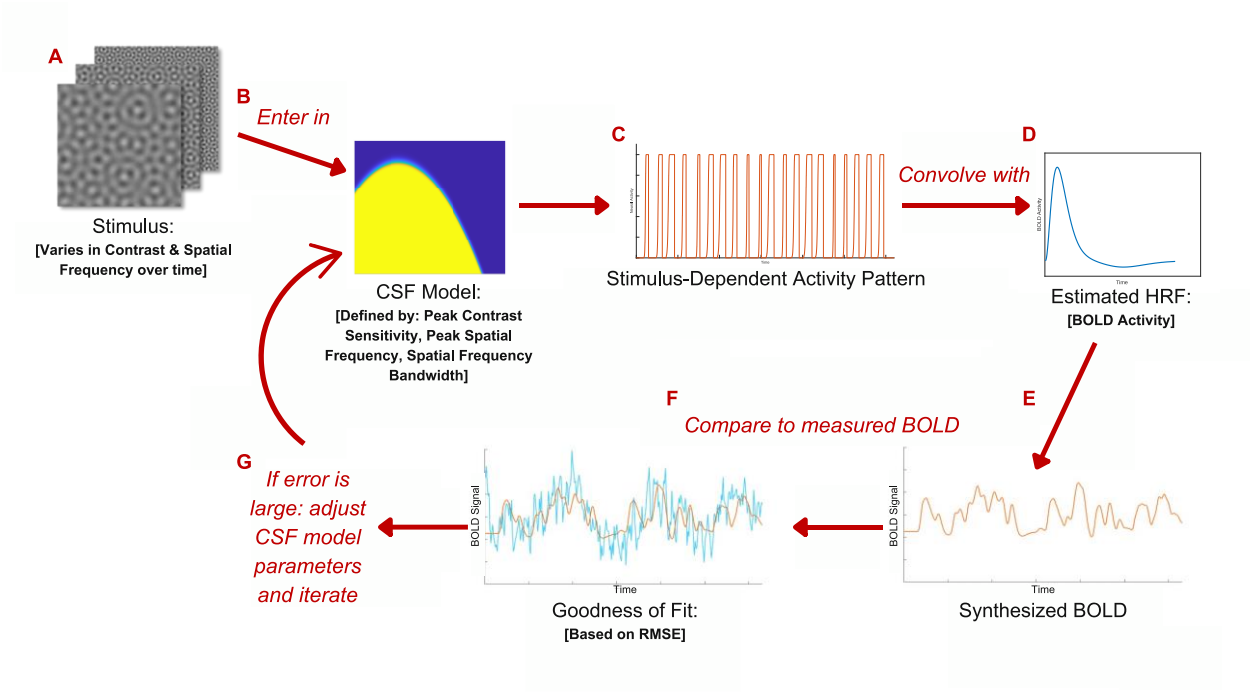

Figure 2. Depiction of the CSF model fitting method. *The procedure begins by assigning a canonical CSF to a voxel (B) and, in consideration of the temporal profile of the stimulus (A), predicting the time-varying voxel response (C). This vector, convolved with the hemodynamic response (D), yields a synthesized fMRI timeseries model (E), which can then be fitted to the measured fMRI data from the voxel (F). If the fit does not sufficiently explain variability in the voxel's time series, we iterate until we converge on a parameter set that best explains the voxel's response (G).*

The different CSF transitions that we presented to the subjects during fMRI scan were recorded along with the contrast, spatial frequency, and the precise transition time (Fig. 2A). The challenge then becomes to identify the CSF model that, when taken into account to generate the model hemodynamic response given the stimulation pattern, explains the bulk of the fMRI response.

The CSF model was estimated by assigning an initial model of the CSF to each voxel, defined by three parameters (i.e., peak contrast sensitivity, peak spatial frequency, spatial frequency bandwidth) (Fig. 2B). The mathematical model of the CSF can be represented by a log-parabola, S'(f), defining sensitivity as [46]:

$$S'(f) = \log_{10}(\gamma_{max}) - \kappa\left(\frac{\log_{10}(f) - \log_{10}(f_{max})}{\beta'/2}\right)^2. \quad (1)$$

Where $\kappa = \log_{10}(2)$, $\beta' = \log_{10}(2\beta)$, γ_{max} represents the peak sensitivity (1/Contrast), f_{max} the peak spatial frequency (cpd) and β the spatial frequency bandwidth (octaves).

In this approach, the CSF model of each voxel was treated similarly to a receptive field representing a boundary in log-log space of contrast sensitivity and spatial frequency. Any time-point of our stimulus (Fig. 2A) represented a shift in this 2-D space of contrast and spatial frequency, such that when the stimulus entered a voxel's receptive field or CSF boundary, and was now suprathreshold, this would elicit a response from the voxel. By calculating the overlap between the stimulus sequence (Fig. 2A) and the CSF model (Fig. 2B), we defined a time-varying voxel response (Fig. 2C). The time-varying voxel response vector was then convolved with a subject-specific and voxel-specific estimated hemodynamic response function (Fig. 2D) to produce a synthesized BOLD timeseries. This produced a function that defined proportional BOLD activity at every time point (Fig. 2E). This model BOLD time-series was then compared to the measured BOLD time-series (Fig. 2F). The difference between the two was calculated using a Goodness of Fit measurement (i.e., RMSE).

If the fit explained variability in the voxel sufficiently, the process stopped, and the parameters of the initial CSF model were saved for that voxel. If not, we searched a parameter

space using a particle swarm optimization algorithm [47-49] and iterated until we converged on the set of CSF parameters that resulted in the best fit between the model and measured BOLD timeseries (Fig. 2G). This process was repeated for every voxel in areas V1, V2, and V3.

Based on the estimated CSF parameters (i.e., peak sensitivity, peak spatial frequency and spatial frequency bandwidth), we then derived voxels' high spatial frequency cutoff from equation 1 by setting $S'(f)$ to 1 and then calculated the associated spatial frequency.

Hemodynamic Response Function (HRF) Estimation

Since the shape of the hemodynamic response function (HRF) can vary significantly between people, we estimated individual HRF for each participant and modeled personalized HRF for each voxel within our region of interest (ROI).

HRF-mapping stimulus

The stimulus consisted of a full field (radius 16◦ visual angle), high contrast texture, consisting of a dynamic, high-contrast pseudo-checkerboard varying in spatial frequency and phase function [50], that briefly appeared on the display for two seconds before returning to a static grey screen for a 20 second period. This cycle was repeated 10 times, totalling one run of approximatively 5 minutes. Participants were instructed to maintain their gaze on a central fixation point (size: 0.1 deg), and to report the color change of the fixation dot.

HRF modelling

The HRF was fitted with the difference of two gamma density functions [51]. The modeled parameters were the time-to-peak of the HRF response and HRF undershoot, the full width at half maximum of the HRF response and HRF undershoot, the ratio adjusting the amplitude of the HRF undershoot relative to the HRF response amplitude, and the scale factor for the final HRF. The

HRF parameters were optimized simultaneously using particle swarm non-linear optimization algorithm.

Retinotopic Atlas ROIs

Surface location and retinotopy estimates (eccentricity and polar angle) of early visual areas (V1,V2, and V3) were obtained by registering a probabilistic retinotopic atlas [52] (https://cfn.upenn.edu/aguirre/wiki/doku.php?id=public:retinotopy_template) to each subject's functional space.

NeuroCSF Voxel Selection

Only voxels with a receptive field center within the range of 0 to 6 degrees of eccentricity were included in the analysis. We also only included gray matter voxels whose coefficient of determination (R^2) was greater than the highest R^2 obtained in any white matter voxel (i.e., use the distribution of R^2 in the white matter as a sample of trivial R^2 values). Based on this method, only voxels with a minimum R^2 of 10% were included in the analysis.

Cross-validation

Each subject was observed with fMRI while viewing three unique runs of our novel stimulus presentation. Each of these runs had a pair with perfectly matched presentation time, for a total of 6 runs. To maximize the R^2 for the fit, we averaged the fMRI data from pairs of runs and thus obtained three measurements of CSF parameters for each voxel. To validate the CSF parameters, we employed leave-one-out-cross-validation (LOOCV) for each voxel in the early visual cortex. Parameters from two pairs of runs were used to predict the time series of another pair of runs, and an average CSF parameter set per voxel was calculated. Cutoff spatial frequency was then derived for each voxel from equation 1.

Results/Figures

Cortical CSF parameters are similar across early visual areas and vary across eccentricity

We first qualitatively assessed the organization of the CSF parameters across the visuocortical map of early visual areas. Parameter estimates were projected onto the cortical surface (Fig. 3) and the visual field maps (Fig. 4-7) to visualize local variations in CSF estimates across the early visual areas and retinal location, respectively.

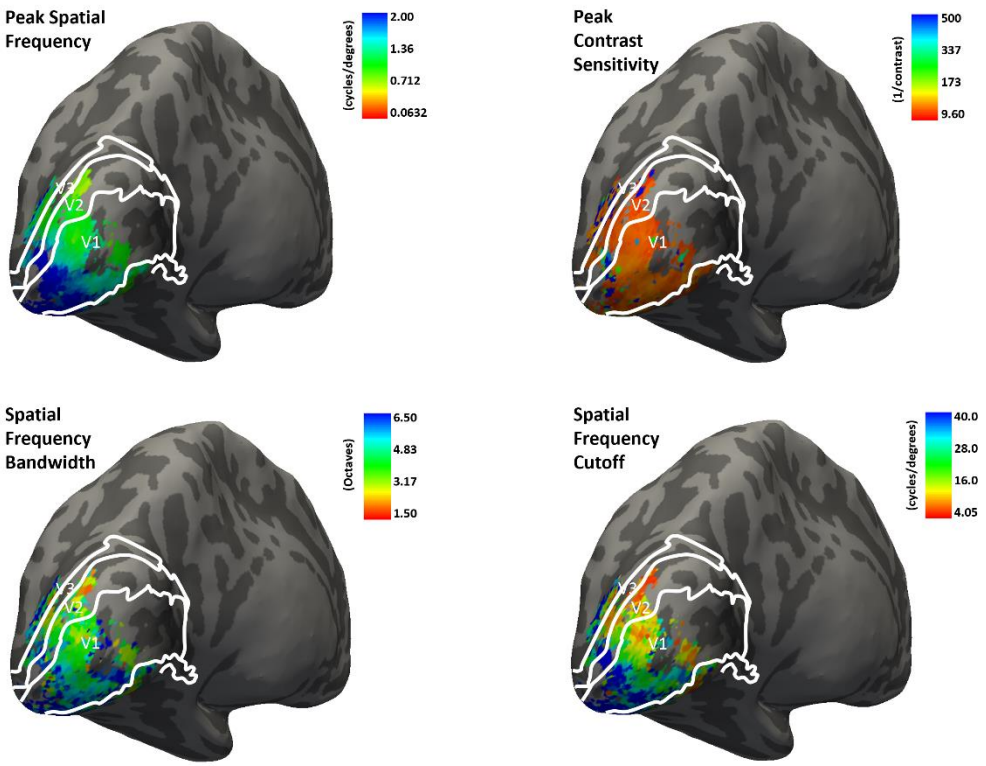

Figure 3. Single subject CSF parameters estimates for subject S03. *Peak contrast sensitivity, peak spatial frequency, spatial frequency bandwidth, and spatial frequency cutoff estimates from 0-6º eccentricity are plotted on the inflated hemisphere of a single subject. Solid white lines indicate the borders between visual areas V1-V2-V3 obtained via Benson, Butt, Datta, Radoeva, Brainard and Aguirre [52].*

For all four parameters, the trends we observed were similar across early visual areas (Fig. 3). We observed systematic changes in peak spatial frequency selectivity with eccentricity. Figure 4 represents the magnitude of the voxel's peak spatial frequency across the visual field for areas V1, V2, V3. Consistent with previous reports [53-56], voxels with foveal retinotopic preferences were

selective for higher spatial frequencies and this peak preference dropped as a function of eccentricity.

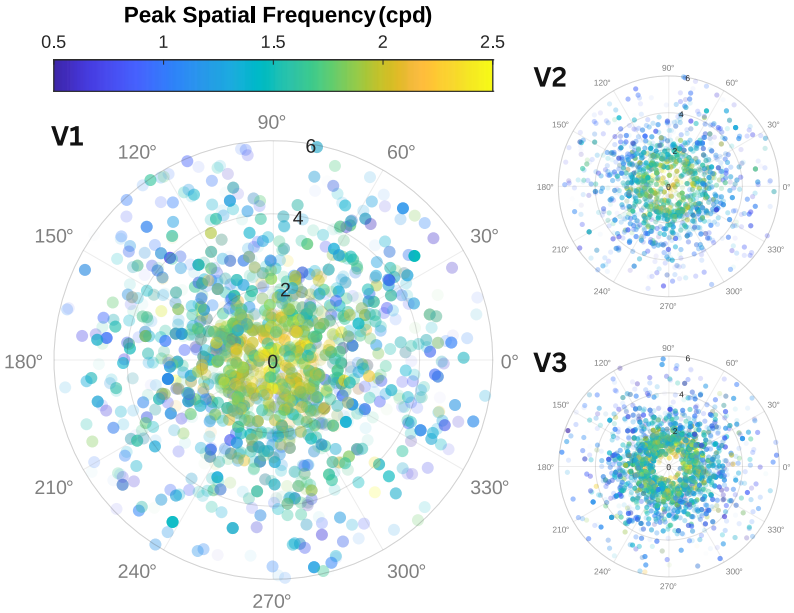

Figure 4. Voxel-wise peak spatial frequency) map across the visual field of early visual cortex. *Each circle represents a single voxel. The magnitude of the voxel's peak spatial frequency in cycles per degree (cpd) is represented by a color code. Color Transparency of the circles are scaled with their coefficient of determination (R^2) value for the neuroCSF fits. Their locations are determined based on their polar angle and eccentricity coordinates. In all 3 visual areas (V1, V2, V3), peak spatial frequency is higher for foveal eccentricity and decreases at parafoveal eccentricities.*

Peak sensitivity values did not show significant shifts with eccentricity across all three visual areas [57-59] (Fig. 5). This result aligns with previous studies, indicating that our stimuli compensated for the reduced cortical representation of peripheral retinal eccentricities [57, 59-61].

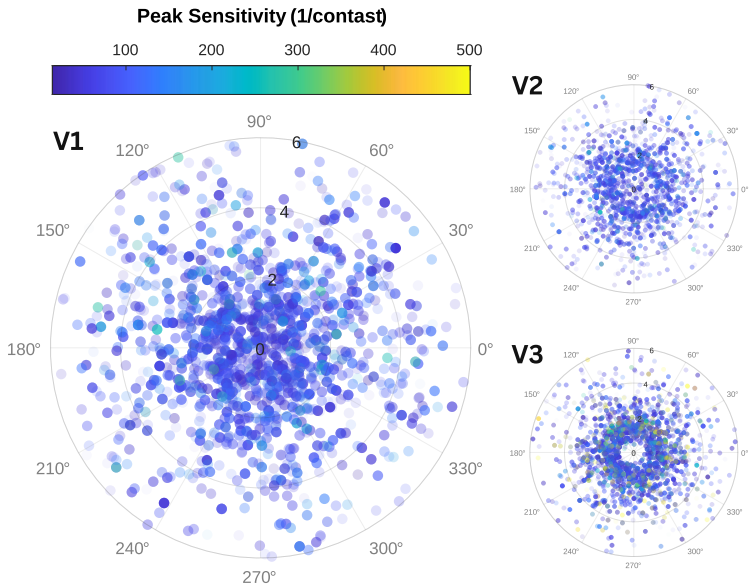

Figure 5. Voxel-wise peak contrast sensitivity map across the visual field of early visual cortex. *Each circle represents a single voxel. The magnitude of the voxel's peak sensitivity (1/contrast) is represented by a color code. Color Transparency of the circles are scaled with their coefficient of determination (R2) value for the neuroCSF fits. Their locations are determined based on their polar angle and eccentricity coordinates. We can see that peak sensitivity values do not shift with eccentricity across all early visual areas (V1, V2, V3).*

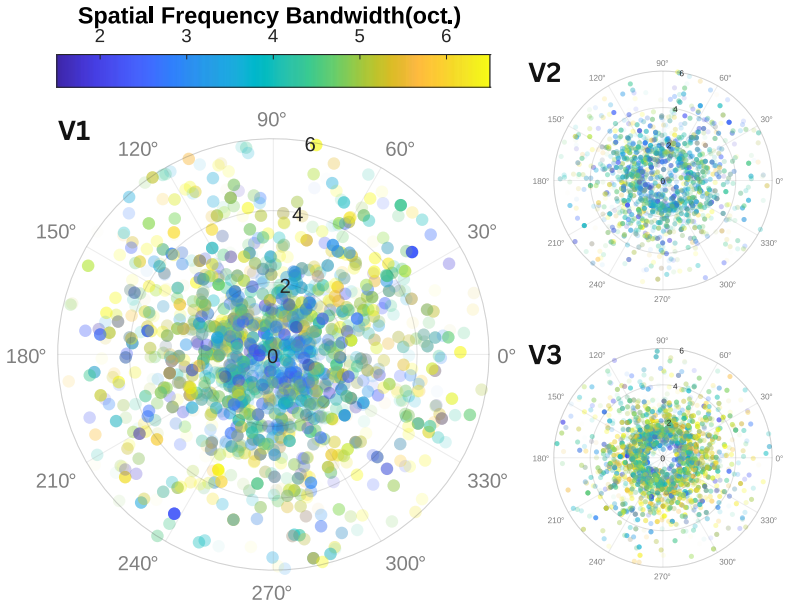

Figure 6. Voxel-wise spatial frequency bandwidth map across the visual field of early visual cortex. *Each circle represents a single voxel. The magnitude of the voxel's spatial frequency bandwidth (octaves) is represented by a color code. Color Transparency of the circles are scaled with their coefficient of determination (R2) value for the neuroCSF fits. Their locations are determined based on their polar angle and eccentricity coordinates. For area V1 and V2, foveal spatial frequency bandwidth is narrower compared to the peripheral region. However, there is no clear trend for V3 voxels.*

We observed a positive trend between spatial frequency bandwidth and retinal eccentricity in V1 and V2 (Fig. 6). However, the relationship was not as clear for V3 voxels. Previous findings from human and animal studies do not predict a clear relationship between spatial frequency bandwidth and eccentricity. While Broderick, Simoncelli and Winawer [56], De Valois, Albrecht and Thorell [62] found that bandwidth is mostly constant across eccentricity, Aghajari, Vinke and Ling [55], Foster, Gaska, Nagler and Pollen [63] only found a moderate increase in bandwidth with eccentricity. In both cases, that increase was more pronounced in V1 compared to higher visual areas. Our results are not inconsistent with those findings.

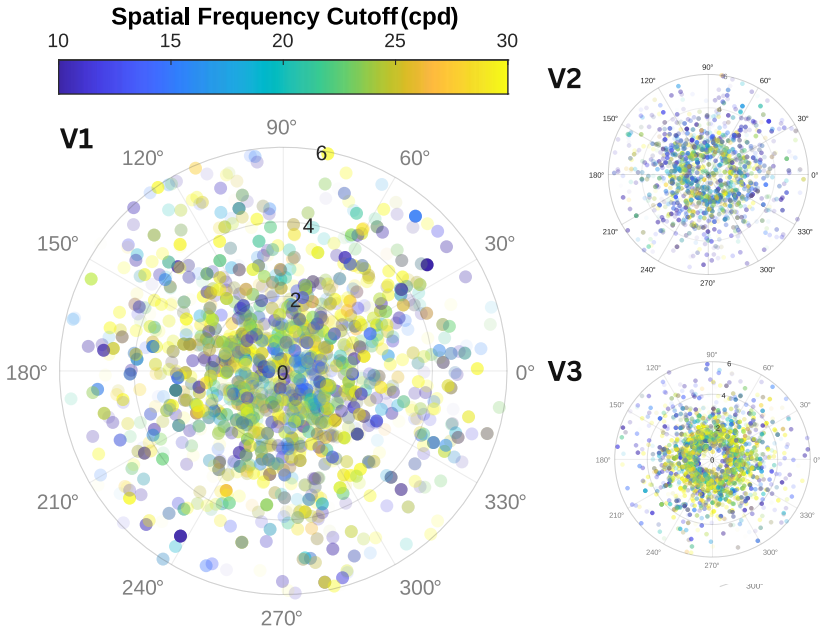

Figure 7. Voxel-wise spatial frequency cutoff map across the visual field of early visual cortex. *Each circle represents a single voxel. The magnitude of the voxel's spatial frequency cutoff (cpd) is represented by a color code. Color Transparency of the circles are scaled with their coefficient of determination (R2) value for the neuroCSF fits. Their locations are determined based on their polar angle and eccentricity coordinates. We cannot see a clear trend between V1 voxels spatial frequency cutoff and eccentricity, while spatial frequency cutoff values decrease with eccentricity across V2 and V3.*

Spatial frequency cutoff showed a modest drop in parafoveal regions compared to foveal regions, primarily in areas V2 and V3 (Fig. 7). High spatial frequency cutoffs remained mostly constant across eccentricities for area V1.

To focus on the eccentricity-based effects, in the next analyses we collapsed our results across polar angles, and we binned the data of our subject into 12 equal sized eccentricity bins from zero to six degrees of visual angle (dva). We looked at the average parameter response as a function of eccentricity and across early visual areas. Previously observed trends were present across all CSF and visual areas (Fig. 8). We found a negative relationship in V1-V3 when examining the average peak spatial frequency [V1: $r(12) = -0.934$, $P < 0.001$; V2: $r(12) = -0.891$ $P < 0.001$; V3: $r(12) = -0.808$, $P < 0.001$] and spatial frequency cutoff [V1: $r(12) = -0.766$, $P < 0.01$; V2: $r(12) = -0.900$, $P < 0.001$; V3: $r(12) = -0.815$, $P < 0.001$] as a function of eccentricity across subjects, (Fig. 8a,d). We observed a positive trend between spatial frequency bandwidth and retinal eccentricity but only for areas V1 and V2 [V1: $r(12) = 0.883$, $P < 0.001$; V2: $r(12) = 0.535$, $P < 0.05$; V3: $r(12) = 0.389$, $P = 0.169$](Fig. 8c). Finally, our analysis didn't reveal any association between peak contrast sensitivity and eccentricity [V1: $r(12) = 0.441$, $P = 0.132$; V2: $r(12) = -0.157$, $P = 0.593$; V3: $r(12) = -0.369$, $P = 0.195$] (Fig. 8b).

We then calculated an average parameters response for foveal (i.e., 0-2 dva) and parafoveal (i.e., 2-6 dva) eccentricities and performed a Wilcoxon Signed-Rank test. With the help of equation 1, we defined CSF curves for foveal and parafoveal eccentricities. Each panel of figure 9 displays two mean CSF curves, one for foveal eccentricities and another for parafoveal eccentricities, for area V1-V2-V3 across all our subjects.

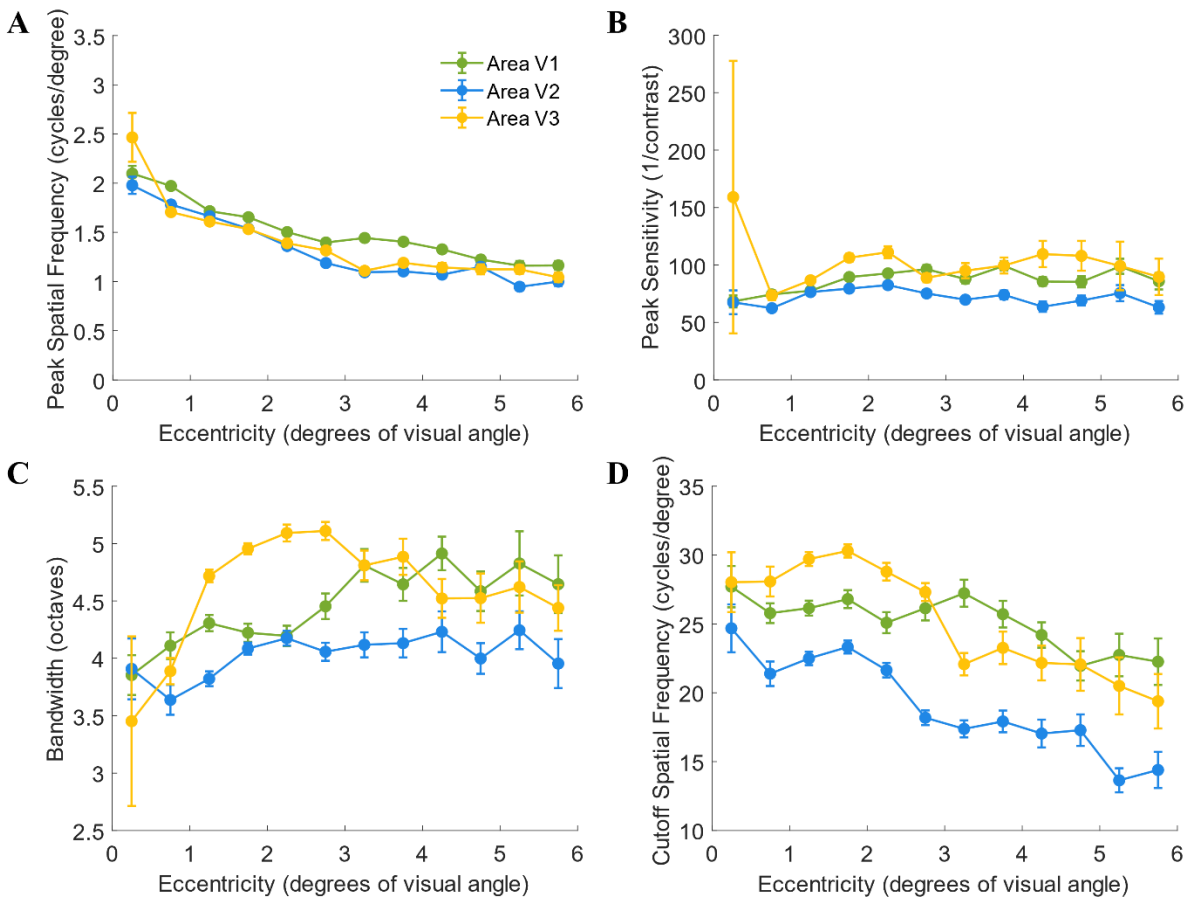

Figure 8. Relationship between the CSF parameters and retinotopic eccentricity across early visual areas. *(A) Mean subject-wise peak spatial frequency estimates within each eccentricity bin. Peak spatial frequency is higher for foveal eccentricity and decreases at parafoveal eccentricities across V1-V2-V3. (B) Mean subject-wise peak sensitivity estimates within each eccentricity bin. Peak gain is stable across eccentricity for all three visual areas. (C) Mean subject-wise spatial frequency bandwidth estimates within each eccentricity bin. Spatial frequency bandwidth slightly increases with eccentricity in area V1 and V3. In area V2, spatial frequency bandwidth is roughly stable across eccentricity. (D) Mean subject-wise spatial frequency cutoff estimates within each eccentricity bin. In V1-V3, mean cutoff values are higher for the fovea compared to parafoveal eccentricities. 12 bins were linearly spaced between the eccentricity range [0.25°,5.75°]. Data from early visual areas (V1, V2, V3) is displayed by a different color. Error bars show the mean ± SE.*

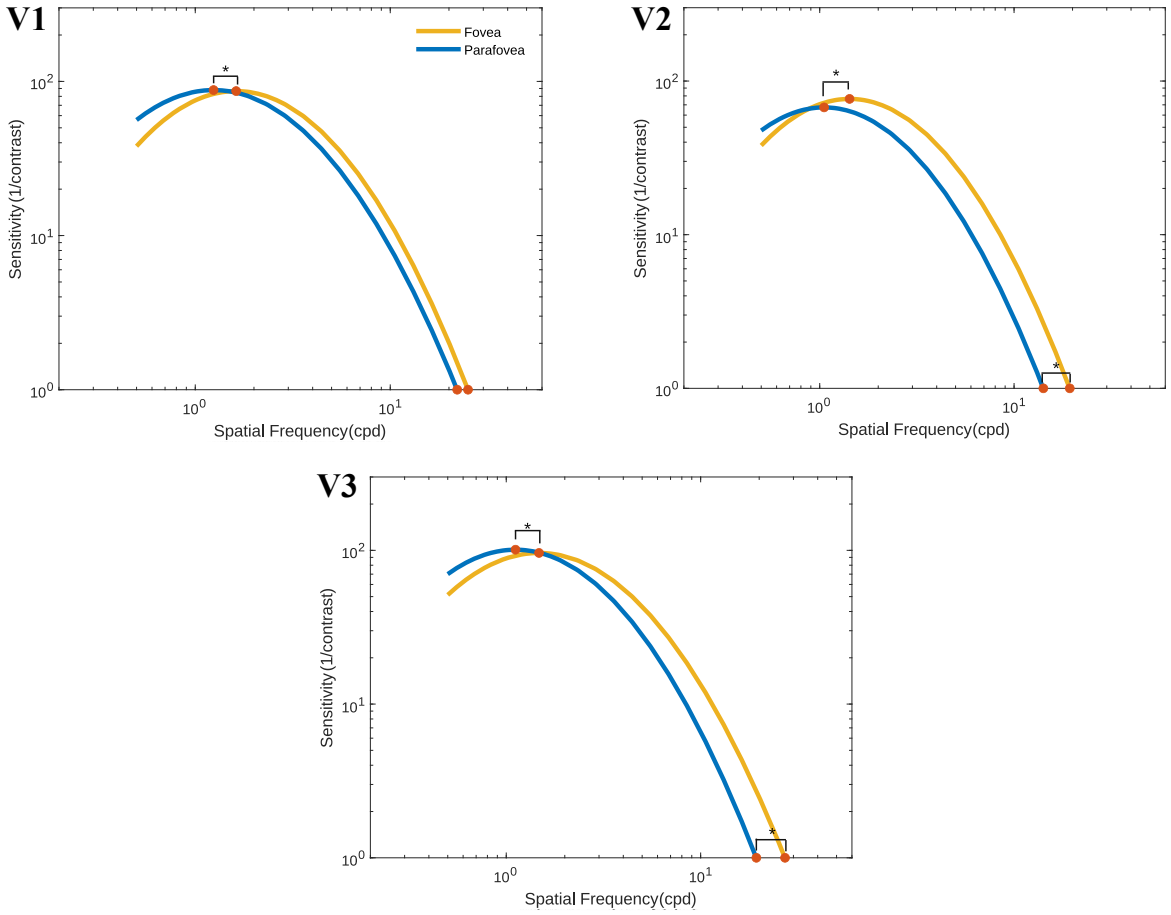

Figure 9. CSF across early visual areas. *Mean subject-wise CSF across areas V1, V2, and V3. Data from foveal and parafoveal eccentricities is displayed by a different color. Significant differences (P < 0.05) between fovea and parafovea are indicated by a (*).*

The results show that there is a statistically significant difference in the mean response of peak spatial frequency between foveal and parafoveal eccentricities in V1-V3 [V1: $Z = -2.521$, $P < 0.05$; V2: $Z = -2.521$, $P < 0.05$; V3: $Z = -2.521$, $P < 0.05$], as well as spatial frequency cutoff in V2-V3 [V1: $Z = -1.260$, $P = 0.208$; V2: $Z = -1.960$, $P < 0.05$; V3: $Z = -2.240$, $P < 0.05$]. However, there were no statistically significant differences in peak contrast sensitivity [V1: $Z = -0.280$, $P = 0.779$; V2: $Z = -1.120$, $P = 0.263$; V3: $Z = -0.140$, $P = 0.889$] and spatial frequency bandwidth [V1: $Z = -1.540$, $P = 0.123$; V2: $Z = -0.840$, $P = 0.401$; V3: $Z = -1.120$, $P = 0.263$] between fovea and parafovea.

Discussion

The neuroCSF is a novel fMRI model-driven approach that combines dynamic stimulation, with a canonical model of the CSF and parameter optimization to provide voxel- wise CSF estimations across early visual areas. With this new method, we were able to derive robust and interpretable estimates of cortical CSF parameters to provide the first complete characterization of the CSF using neuroimaging data. Our approach provides estimates of four parameters per visual field location: peak gain, peak spatial frequency, spatial frequency bandwidth, and the cut-off frequency of the CSF.

One of the major concerns of vision neuroscience is to relate the organization of cortical processing to perception. Psychophysical studies have consistently shown that behavioral measures of contrast and spatial frequency sensitivities decrease from foveal to peripheral eccentricities. Previous neuroimaging and neurophysiological studies independently estimated human spatial frequency tuning [53, 55, 56, 64, 65] and contrast sensitivity [66, 67] across the visual cortex. To our knowledge, the neuroCSF is the first human neuroimaging approach that unifies these measurements. This integration allowed us to explore the spatial organization of the CSF across early visual areas to provide valuable insights into the relationship between behavioral CSF measurements and their cortical counterparts. The dependency of CSF parameters on retinotopy and eccentricity that we found in all three visual areas was consistent with prior studies [55, 56, 62, 63, 68, 69]. Our results support Aghajari, Vinke and Ling [55,] Movshon, Thompson and Tolhurst [68,] Campbell, Cooper and Enroth-Cugell [69] findings, suggesting a fast rate of peak spatial frequency decline with eccentricity across V1-V3. Spatial frequency bandwidth changes were similar across V1&V3, with larger values in peripheral eccentricity. Spatial frequency bandwidth remained relatively consistent across eccentricity for V2. These results match previous conflicting reports

of the relationship between spatial frequency selectivity and eccentricity [55, 56, 62, 63]. Aghajari, Vinke and Ling [55] noted a slight increase in bandwidth with eccentricity but only for the perifovea. Since we only sampled the fovea and parafovea this could explain why we didn't detect a similar trend between spatial frequency selectivity and eccentricity. These results can help resolve some of the discrepancies in the literature regarding spatial frequency selectivity and eccentricity.

Peak gain was found to be independent of eccentricity across V1-V3. By using full field stimuli, we ensured the cortical representation of the gratings at various eccentricities became equal in size, compensating for the reduced cortical representation that usually limits contrast sensitivity in the periphery [57, 59-61, 70]. Similarly to Broderick, Simoncelli and Winawer [56], our results did not reveal a significant trend between spatial frequency cutoff and eccentricity for area V1. However, we did find a significant effect of eccentricity on the cutoff for V2-V3. Our findings aligned with established behavioral trends, thus reinforcing the link between cortical anatomy and perceptual abilities.

Our approach differs from existing methods to measure human CSF in that it overcomes measurement trade-offs and patient limitations, while also presenting pathophysiological relevance. Traditional approaches to measuring the human CSF face trade-offs between precision and testing time, limiting their utility. When sampling the two-dimensional space of possible stimuli- defined by contrast and spatial frequency- the range of stimuli needs to be wide enough to capture the global shape of the CSF, but it also needs to be precise enough to capture the highly dynamic regions of the curve such as the high-frequency cutoff. To improve the flexibility and precision of traditional CSF tests, sampling range needs to be increased, but this would introduce the cost of extra testing time. In contrast, with our model-driven approach that is combined with dynamic stimuli, we can sweep through a wide range of spatial frequency and contrast across the

visual field over a short period of time. This strategy allows for a wide sampling range and resolution without increased testing time.

Our approach differs from existing methods to measure human CSF in that it overcomes measurement trade-offs and patient limitations, while also presenting pathophysiological relevance.

Traditional approaches to measuring the human CSF face trade-offs between precision and testing time, limiting their utility. When sampling the two-dimensional space of possible stimuli- defined by contrast and spatial frequency- the range of stimuli needs to be wide enough to capture the global shape of the CSF, but it also needs to be precise enough to capture the highly dynamic regions of the curve such as the high-frequency cutoff. Traditional approaches present fixed and pre-selected numbers of contrast and spatial frequency levels that are measured several times at one or multiple eccentricities. To improve the flexibility and precision of current CSF tests, sampling range needs to be increased, but this would introduce the cost of extra testing time. In other words, conventional CSF measurements can either be precise or fast, but not both. In contrast, with our model-driven approach that is combined with dynamic stimuli, we can sweep through a wide range of spatial frequency and contrast across the visual field over a short period of time. This strategy allows for a wide sampling range and resolution without increased testing time.

Current methods to measure the CSF can be challenging for healthy participants, and even more so for patients who suffer from attention or fixation problems and visual discomfort [71, 72]. These factors can also influence the reliability of current behavioral CSF measures [30-33]. With its use of a full field stimuli, neuroCSF eliminates the need for participant fixation. Our novel

technique also estimates the CSF without the need for participant input, making it suitable for nonverbal individuals like infants or those with intellectual disabilities.

While neuroCSF offers advantages in stimulus flexibility, optimizing stimulus designs to accurately capture the complete CSF profile is not without challenges. Balancing the range and resolution of stimuli while minimizing testing time remains a methodological concern that needs careful consideration. Next iterations of the stimulus could be more targeted to reduce the scanning time. We are currently working on an optimization approach to define a set of stimuli that yields the most information about the CSF's overall shape.

Although the neuroCSF technique provides valuable insights into cortical CSF parameters, its relationship to traditional behavioral CSF measures should be further validated. Understanding the degree of correspondence between neuroimaging-derived CSF estimates and psychophysical measurements is crucial for establishing its reliability and validity.

The neuroCSF technique relies on a log-parabolic model to describe CSF parameters. This model of the CSF is a simplified version of the truncated log-parabola that has previously been used in psychophysical studies to estimate CSF parameters [46, 71, 73, 74], and has been shown to provide, compared to other models, excellent fits with very few assumptions, parameters and calculations [46, 75-77]. While this model simplifies the estimation process, it may not fully capture all the nuances of individual differences or variations in CSF profiles. The symmetric log-parabola typically misfits the plateau observed on the peak's low-frequency side [78]. This could constrain the model's accuracy in specific cases. With an additional parameter to describe the low-frequency plateau, the truncated log-parabola can deal with the issues of the CSF's asymmetry.

Addressing these limitations and conducting further research to mitigate their impact will be essential for harnessing the full potential of the neuroCSF technique.

References

1. Campbell FW, Robson JG. Application of Fourier analysis to the visibility of gratings. *J Physiol* 1968;197:551-566.
2. Vision NRCCo. *Emergent Techniques for Assessment of Visual Performance.* Washington (DC): National Academies Press (US)
Copyright © National Academy of Sciences.; 1985.
3. Gervais MJ, Harvey LO, Jr., Roberts JO. Identification confusions among letters of the alphabet. *J Exp Psychol Hum Percept Perform* 1984;10:655-666.
4. Owsley C, Sloane ME. Contrast sensitivity, acuity, and the perception of 'real-world' targets. *Br J Ophthalmol* 1987;71:791-796.
5. West SK, Rubin GS, Broman AT, Muñoz B, Bandeen-Roche K, Turano K. How does visual impairment affect performance on tasks of everyday life? The SEE Project. Salisbury Eye Evaluation. *Arch Ophthalmol* 2002;120:774-780.
6. Stalin A, Dalton K. Relationship of Contrast Sensitivity Measured Using Quick Contrast Sensitivity Function With Other Visual Functions in a Low Vision Population. *Investigative ophthalmology & visual science* 2020;61:21-21.
7. Legge GE, Rubin GS, Pelli DG, Schleske MM. Psychophysics of reading—II. Low vision. *Vision Research* 1985;25:253-265.
8. Lovie-Kitchin J, Mainstone J, Robinson J, Brown B. What areas of of the visual field are important for mobility in low vision patients. *Clinical vision sciences* 1990.
9. Woods RL, Wood JM. The role of contrast sensitivity charts and contrast letter charts in clinical practice. *Clinical and Experimental Optometry* 1995;78:43-57.
10. Marron JA, Bailey IL. Visual factors and orientation-mobility performance. *Am J Optom Physiol Opt* 1982;59:413-426.
11. Arden GB. The importance of measuring contrast sensitivity in cases of visual disturbance. *British Journal of Ophthalmology* 1978;62:198-209.
12. Jindra LF, Zemon V. Contrast sensitivity testing: A more complete assessment of vision. *Journal of Cataract & Refractive Surgery* 1989;15:141-148.
13. Wang G, Zhao C, Ding Q, Wang P. An Assessment of the Contrast Sensitivity in Patients with Ametropic and Anisometropic Amblyopia in Achieving the Corrected Visual Acuity of 1.0. *Scientific Reports* 2017;7:42043.
14. Chatzistefanou KI, Theodossiadis GP, Damanakis AG, Ladas ID, Moschos MN, Chimonidou E. Contrast sensitivity in amblyopia: the fellow eye of untreated and successfully treated amblyopes. *J aapos* 2005;9:468-474.
15. Wong WL, Su X, Li X, et al. Global prevalence of age-related macular degeneration and disease burden projection for 2020 and 2040: a systematic review and meta-analysis. *Lancet Glob Health* 2014;2:e106-116.
16. Owsley C, Huisingh C, Clark ME, Jackson GR, McGwin G, Jr. Comparison of Visual Function in Older Eyes in the Earliest Stages of Age-related Macular Degeneration to Those in Normal Macular Health. *Curr Eye Res* 2016;41:266-272.

17. Cocce KJ, Stinnett SS, Luhmann UFO, et al. Visual Function Metrics in Early and Intermediate Dry Age-related Macular Degeneration for Use as Clinical Trial Endpoints. *Am J Ophthalmol* 2018;189:127-138.
18. Klein R, Wang Q, Klein BE, Moss SE, Meuer SM. The relationship of age-related maculopathy, cataract, and glaucoma to visual acuity. *Invest Ophthalmol Vis Sci* 1995;36:182-191.
19. Hoffmann L, Rossouw P, Guichard MM, Hatz K. Strongest Correlation Between Contrast Sensitivity and Morphological Characteristics in Bilateral nAMD. *Front Med (Lausanne)* 2020;7:622877.
20. Chung ST, Legge GE. Comparing the Shape of Contrast Sensitivity Functions for Normal and Low Vision. *Invest Ophthalmol Vis Sci* 2016;57:198-207.
21. Kleiner RC, Enger C, Alexander MF, Fine SL. Contrast sensitivity in age-related macular degeneration. *Arch Ophthalmol* 1988;106:55-57.
22. Chen L, Gordon LK. Ocular manifestations of multiple sclerosis. *Current Opinion in Ophthalmology* 2005;16:315-320.
23. McDonald WI, Barnes D. The ocular manifestations of multiple sclerosis. 1. Abnormalities of the afferent visual system. *J Neurol Neurosurg Psychiatry* 1992;55:747-752.
24. Jackson TL, Ong GL, Ripley LG. Orientational contrast sensitivity and chromatic contrast thresholds in multiple sclerosis. *Am J Ophthalmol* 2004;137:283-286.
25. Nunes AF, Monteiro PM, Vaz Pato M. Influence of multiple sclerosis, age and degree of disability, in the position of the contrast sensitivity curve peak. *Indian J Ophthalmol* 2014;62:180-185.
26. Ripley DL, Politzer T. Vision disturbance after TBI. *NeuroRehabilitation* 2010;27:215-216.
27. Collins MW, Kontos AP, Okonkwo DO, et al. Statements of Agreement From the Targeted Evaluation and Active Management (TEAM) Approaches to Treating Concussion Meeting Held in Pittsburgh, October 15-16, 2015. *Neurosurgery* 2016;79:912-929.
28. Kelly DH, Savoie RE. A study of sine-wave contrast sensitivity by two psychophysical methods. *Perception & Psychophysics* 1973;14:313-318.
29. Harvey LO, Jr. Efficient estimation of sensory thresholds with ML-PEST. *Spat Vis* 1997;11:121-128.
30. Abramov I, Hainline L, Turkel J, et al. Rocket-ship psychophysics. Assessing visual functioning in young children. *Invest Ophthalmol Vis Sci* 1984;25:1307-1315.
31. Bradley A, Freeman RD. Contrast sensitivity in children. *Vision Research* 1982;22:953-959.
32. Lee TH, Baek J, Lu ZL, Mather M. How arousal modulates the visual contrast sensitivity function. *Emotion* 2014;14:978-984.
33. Abrahamyan A, Silva LL, Dakin SC, Carandini M, Gardner JL. Adaptable history biases in human perceptual decisions. *Proceedings of the National Academy of Sciences* 2016;113:E3548-E3557.
34. Thomas J. Normal and amblyopic contrast sensitivity function in central and peripheral retinas. *Invest Ophthalmol Vis Sci* 1978;17:746-753.
35. Katz LM, Levi DM, Bedell HE. Central and peripheral contrast sensitivity in amblyopia with varying field size. *Doc Ophthalmol* 1984;58:351-373.

36. Midena E, Pilotto E. Microperimetry in age: related macular degeneration. *Eye* 2017;31:985-994.
37. Lopes de Faria JM, Katsumi O, Arai M, Hirose T. Objective measurement of contrast sensitivity function using contrast sweep visual evoked responses. *The British journal of ophthalmology* 1998;82:168-173.
38. Hemptinne C, Liu-Shuang J, Yuksel D, Rossion B. Rapid Objective Assessment of Contrast Sensitivity and Visual Acuity With Sweep Visual Evoked Potentials and an Extended Electrode Array. *Investigative Ophthalmology & Visual Science* 2018;59:1144-1157.
39. Howe JW, Mitchell KW. The objective assessment of contrast sensitivity function by electrophysiological means. *British Journal of Ophthalmology* 1984;68:626-638.
40. Mooney SWJ, Alam NM, Hill NJ, Prusky GT. Gradiate: A radial sweep approach to measuring detailed contrast sensitivity functions from eye movements. *Journal of Vision* 2020;20:17-17.
41. Dakin SC, Turnbull PRK. Similar contrast sensitivity functions measured using psychophysics and optokinetic nystagmus. *Scientific Reports* 2016;6:34514.
42. Jones PR, Kalwarowsky S, Atkinson J, Braddick OJ, Nardini M. Automated Measurement of Resolution Acuity in Infants Using Remote Eye-Tracking. *Investigative Ophthalmology & Visual Science* 2014;55:8102-8110.
43. Brainard DH. The Psychophysics Toolbox. *Spat Vis* 1997;10:433-436.
44. Farivar R, Grigorov F, van der Kouwe AJ, Wald LL, Keil B. Dense, shape-optimized posterior 32-channel coil for submillimeter functional imaging of visual cortex at 3T. *Magn Reson Med* 2016;76:321-328.
45. Cox RW. AFNI: software for analysis and visualization of functional magnetic resonance neuroimages. *Comput Biomed Res* 1996;29:162-173.
46. Watson AB, Ahumada AJ, Jr. A standard model for foveal detection of spatial contrast. *Journal of Vision* 2005;5:6-6.
47. Ab Wahab MN, Nefti-Meziani S, Atyabi A. A comprehensive review of swarm optimization algorithms. *PLoS One* 2015;10:e0122827.
48. Helwig S, Branke J, Mostaghim SM. Experimental Analysis of Bound Handling Techniques in Particle Swarm Optimization. *IEEE Transactions on Evolutionary Computation* 2013;17.
49. Mendes R, Kennedy J, Neves J. The fully informed particle swarm: simpler, maybe better. *IEEE Transactions on Evolutionary Computation* 2004;8.
50. Alvarez I, De Haas B, Clark C, Rees G, Schwarzkopf D. Comparing different stimulus configurations for population receptive field mapping in human fMRI. *Frontiers in Human Neuroscience* 2015;9.
51. Worsley KJ, Liao CH, Aston J, et al. A general statistical analysis for fMRI data. *Neuroimage* 2002;15:1-15.
52. Benson NC, Butt OH, Datta R, Radoeva PD, Brainard DH, Aguirre GK. The Retinotopic Organization of Striate Cortex Is Well Predicted by Surface Topology. *Current Biology* 2012;22:2081-2085.
53. Henriksson L, Nurminen L, Hyvärinen A, Vanni S. Spatial frequency tuning in human retinotopic visual areas. *Journal of Vision* 2008;8:5-5.

54. Hess RF, Li X, Mansouri B, Thompson B, Hansen BC. Selectivity as well as sensitivity loss characterizes the cortical spatial frequency deficit in amblyopia. *Hum Brain Mapp* 2009;30:4054-4069.
55. Aghajari S, Vinke LN, Ling S. Population spatial frequency tuning in human early visual cortex. *Journal of Neurophysiology* 2020;123:773-785.
56. Broderick WF, Simoncelli EP, Winawer J. Mapping spatial frequency preferences across human primary visual cortex. *Journal of Vision* 2022;22:3-3.
57. Himmelberg MM, Winawer J, Carrasco M. Stimulus-dependent contrast sensitivity asymmetries around the visual field. *Journal of Vision* 2020;20:18-18.
58. Rovamo J, Franssila R, Näsänen R. Contrast sensitivity as a function of spatial frequency, viewing distance and eccentricity with and without spatial noise. *Vision Res* 1992;32:631-637.
59. Rovamo J, Virsu V, NÄSÄNen R. Cortical magnification factor predicts the photopic contrast sensitivity of peripheral vision. *Nature* 1978;271:54-56.
60. Rovamo J, Virsu V. An estimation and application of the human cortical magnification factor. *Experimental Brain Research* 1979;37:495-510.
61. Virsu V, Rovamo J. Visual resolution, contrast sensitivity, and the cortical magnification factor. *Experimental Brain Research* 1979;37:475-494.
62. De Valois RL, Albrecht DG, Thorell LG. Spatial frequency selectivity of cells in macaque visual cortex. *Vision Res* 1982;22:545-559.
63. Foster KH, Gaska JP, Nagler M, Pollen DA. Spatial and temporal frequency selectivity of neurones in visual cortical areas V1 and V2 of the macaque monkey. *J Physiol* 1985;365:331-363.
64. Sirovich L, Uglesich R. The organization of orientation and spatial frequency in primary visual cortex. *Proceedings of the National Academy of Sciences* 2004;101:16941-16946.
65. Singh KD, Smith AT, Greenlee MW. Spatiotemporal Frequency and Direction Sensitivities of Human Visual Areas Measured Using fMRI. *Neuroimage* 2000;12:550-564.
66. Himmelberg MM, Wade AR. Eccentricity-dependent temporal contrast tuning in human visual cortex measured with fMRI. *Neuroimage* 2019;184:462-474.
67. Marquardt I, Schneider M, Gulban OF, Ivanov D, Uludağ K. Cortical depth profiles of luminance contrast responses in human V1 and V2 using 7 T fMRI. *Hum Brain Mapp* 2018;39:2812-2827.
68. Movshon JA, Thompson ID, Tolhurst DJ. Spatial and temporal contrast sensitivity of neurones in areas 17 and 18 of the cat's visual cortex. *J Physiol* 1978;283:101-120.
69. Campbell FW, Cooper GF, Enroth-Cugell C. The spatial selectivity of the visual cells of the cat. *J Physiol* 1969;203:223-235.
70. Horton JC, Hoyt WF. The Representation of the Visual Field in Human Striate Cortex: A Revision of the Classic Holmes Map. *Archives of Ophthalmology* 1991;109:816-824.
71. Lesmes LA, Lu ZL, Baek J, Albright TD. Bayesian adaptive estimation of the contrast sensitivity function: the quick CSF method. *J Vis* 2010;10:17.11-21.
72. Kalia A, Lesmes LA, Dorr M, et al. Development of pattern vision following early and extended blindness. *Proceedings of the National Academy of Sciences* 2014;111:2035-2039.
73. Rosenkranz SC, Kaulen B, Zimmermann HG, Bittner AK, Dorr M, Stellmann J-P. Validation of Computer-Adaptive Contrast Sensitivity as a Tool to Assess Visual Impairment in Multiple Sclerosis Patients. *Frontiers in Neuroscience* 2021;15.

74. Tardif J, Watson MR, Giaschi D, Gosselin F. The Curve Visible on the Campbell-Robson Chart Is Not the Contrast Sensitivity Function. *Frontiers in Neuroscience* 2021;15.
75. Spiegel DP, Reynaud A, Ruiz T, Laguë-Beauvais M, Hess R, Farivar R. First- and second-order contrast sensitivity functions reveal disrupted visual processing following mild traumatic brain injury. *Vision Res* 2016;122:43-50.
76. Gao Y, Reynaud A, Tang Y, Feng L, Zhou Y, Hess RF. The amblyopic deficit for 2nd order processing: Generality and laterality. *Vision Research* 2015;114:111-121.
77. Reynaud A, Tang Y, Zhou Y, Hess RF. A normative framework for the study of second-order sensitivity in vision. *Journal of Vision* 2014;14:3-3.
78. Rohaly AM, Owsley C. Modeling the contrast-sensitivity functions of older adults. *J Opt Soc Am A* 1993;10:1591-1599.